Industrial Chemistry & Materials

ROYAL SOCIETY OF CHEMISTRY

PAPER

View Article Online
View Journal

Open Access Article. Published on 15 December 2025. Downloaded on 2/5/2026 10:57:16 PM.
This article is licensed under a Creative Commons Attribution-NonCommercial 3.0 Unported Licence.

Check for updates

Cite this: DOI: 10.1039/d5im00245a

Dual kinetic effect from confined iron nanoparticles in zeolite modulates high-temperature catalytic NO reduction and NH_3 oxidation

Xinlin Xie, Jibin Yuan, Lei Liu, Hanzi Liu* and Zhiqiang Sun *

The selective catalytic reduction of ammonia (NH_3-SCR) is a promising technology for abating nitrogen oxides (NO_x), yet its application at high temperatures is severely hampered by the over-oxidation of ammonia, leading to a trade-off between NO_x conversion and N_2 selectivity. Herein, we construct a series of Fe-exchanged ZSM-5 catalysts with controlled Fe loadings (0.05–0.5 wt%) to decouple the competing reaction pathways. The optimized 0.1Fe@ZSM-5 catalyst achieves 83.0% NO_x conversion at 700 °C and maintains exceptional stability for over 120 h under harsh conditions, representing a significant performance enhancement. Mechanistic investigations combining kinetic modeling and *in situ* spectroscopy reveal a dual kinetic regime, governed by the size of the Fe species. Catalysts with low Fe loadings favor the standard SCR pathway *via* stable NH_4^+ and NH_2^* intermediates, whereas catalysts with higher loadings and larger Fe nanoparticles promote the undesirable oxidation of ammonia to NO_x. The result identifies that the optimal catalytic sites for high-temperature SCR rely on a delicate balance, activating ammonia for the desired reaction while suppressing its subsequent over-oxidation. These findings provide new implications for advanced catalyst design by tuning the active site structure to navigate competing reaction kinetics.

Received 12th September 2025,
Accepted 1st December 2025

DOI: 10.1039/d5im00245a

rsc.li/icm

Keywords: Selective catalytic reduction; NH_3 oxidation; Kinetics modeling; Brønsted acid site; N_2 selectivity.

1 Introduction

The abatement of nitrogen oxides (NO_x) from high-temperature exhaust streams is a critical challenge in emerging industrial scenarios, including the after-treatment of diesel engine emissions, end-of-pipe control for ammonia–hydrogen co-firing, and the management of emissions from coal-fired boilers under rapid load changes.[1,2] The selective catalytic reduction of NO_x with ammonia (NH_3-SCR) over Fe-based zeolites represents a promising technology due to its exceptional efficacy in promoting NH_3 dehydrogenation and N–N bond formation.[3] However, the catalysts are susceptible to deactivation by sulfur poisoning and hydrothermal aging.[4] More critically, the over-oxidation of ammonia at elevated temperatures severely suppresses the overall NO_x reduction activity.[5–8] Our previous work has shown that incorporating transition metals can enhance thermal-sulfur stability through synergistic effects;[9] however, a fundamental understanding of the NH_3 oxidation mechanism and its kinetics at high temperatures remains elusive. Specifically, suppressing ammonia over-oxidation above 700 °C with sufficient deNO_x efficiency shows a significant yet challenging task.

The catalytic oxidation of ammonia over metal-based catalysts has been studied extensively, both for its abatement as a toxic pollutant and for its potential in chemical synthesis, yielding products such as N_2, NO, and N_2O.[10–12] The ammonia activation is facilitated by metal–oxygen sites *via* abstraction of a H^+ proton, where the stronger oxidizability of the metal–oxygen bonds plays a crucial role. For instance, iron oxides possess a relatively low Fe–O bond energy, enabling the activation of NH_3. In the case of NH_3-SCR, rational ammonia oxidation is beneficial, as it accelerates the initial dehydrogenation to form the NH_2^* intermediate, which couples with NO to produce N_2. However, under excessively oxidizing conditions, lattice oxygen can drive the progressive dehydrogenation of adsorbed NH_2^*. This process leads to the formation of highly reactive NH* or N* radicals, which are subsequently oxidized to NO_x, thereby lowering

Hunan Engineering Research Center of Clean and Low-Carbon Energy Technology, School of Energy Science and Engineering, Central South University, Changsha 410083, China. E-mail: liuhz@csu.edu.cn, zqsun@csu.edu.cn

© 2025 The Author(s). Co-published by the Institute of Process Engineering, Chinese Academy of Sciences and the Royal Society of Chemistry

Open Access Article. Published on 15 December 2025. Downloaded on 2/5/2026 10:57:16 PM. This article is licensed under a Creative Commons Attribution-NonCommercial 3.0 Unported Licence.

the N_2 selectivity and suppressing the catalytic performance for the desired NO_x reduction.[13,14] This inherent trade-off between NH_3 conversion and N_2 selectivity poses a challenge for NH_3-SCR reactions on activated metal oxide surfaces.

Fe-based zeolites are energetically favored for stable NO reduction and high N_2 selectivity, owing to their inherent spatial confinement and shape-selective properties.[7] Previous studies have focused on the kinetics and mechanisms of the interaction between NO_x and NH_3.[15,16] According to acid–base principles, the exchange of Fe ions into the zeolite framework generates Brønsted acid sites associated with Fe–OH moieties, which are recognized as critical for the initial adsorption and activation of NH_3, thereby facilitating N–N bond coupling.[17,18] However, an excessive concentration of these exposed acid sites can trigger the over-oxidation of ammonia. Current research often investigates how the catalyst's lattice structure, oxidation state, and acid site distribution influence NO conversion and N_2 selectivity, with the reaction pathway of NH_2NO^* being a key intermediate.[19–22] Recent work has demonstrated the local coordination structure of the metal sites in dictating the diffusion pathways of dehydrogenated species, where van der Waals forces can create a barrier effect that suppresses the egress of intermediates leading to side reactions.[23] The disparity between Fe–O and Si–O bond lengths makes the Fe catalytic center particularly sensitive to local defects, which in turn alters the Fe–Fe and Fe–O coordination environments and the structure of the Fe–OH acid sites. By tailoring the oxidative properties and coordination environment of the catalytic Fe centers, one can modulate the product selectivity and reaction network through synergistic kinetics. Therefore, establishing a quantitative descriptor that correlates Fe–Fe/O coordination numbers and acid properties helps to fundamentally decouple the competing pathways of NO reduction and NH_3 oxidation.

In this study, we report the synthesis and robust catalytic performance of a series of Fe-exchanged ZSM-5 catalysts. By developing a comprehensive kinetic model that couples the primary SCR reaction with parasitic NH_3 oxidation, we demonstrate that the ion-exchanged Fe loading directly affects the high-temperature NH_3–NO–O_2 reaction system. Among the catalysts studied, 0.1Fe@ZSM-5 achieved a NO conversion of 83.0% and maintained exceptional stability for over 120 h at 700 °C in the presence of SO_2 and water vapor. This performance represents a 15.2% enhancement in high-temperature de-NO_x activity at 850 °C compared to our previous work. Mechanistically, we reveal that the exposed Fe nanoparticles facilitate the consumption of NH_3-coordinated Lewis acid sites, promoting NH_3 adsorption and activation on the Brønsted acid sites for the SCR reaction. Simultaneously, these nanoparticles catalyze further dehydrogenation of NH_2^* intermediates at elevated temperatures, which leads to the undesired over-oxidation of ammonia to NO.

2 Results and discussion

2.1 Characterization of Fe@ZSM-5

The Fe@ZSM-5 catalysts were synthesized *via* a facile ion-exchange method, schematically depicted in Fig. 1a. A series of catalysts with different iron mass loadings were prepared and are denoted as 0.05Fe@ZSM-5, 0.08Fe@ZSM-5, 0.1Fe@ZSM-5, and 0.5Fe@ZSM-5, based on the calculated Fe content during synthesis. The loading of Fe was determined by ICP-OES and the results are summarized in Table S1. Detailed synthesis procedures are provided in the Experimental and computational section. Unless otherwise specified, HZSM-5 in this work refers to the zeolite with a Si/Al ratio of 27. X-ray diffraction (XRD) patterns confirmed the retention of the MFI framework, showing characteristic reflections at 8.1° (101) and 23.2° (332) (Fig. 1b). Notably, no diffraction peaks corresponding to Fe_2O_3 (*e.g.*, at 33.2°, 35.7°, or 53.6°) or other crystalline iron-containing phases were detected,[24,25] indicating the dispersed state of iron species on the ZSM-5 lattice.

Transmission electron microscopy (TEM) revealed the microstructural features of 0.5Fe@ZSM-5 (Fig. 1c, S1 and S2). The large-scale image displays the characteristic morphology of the MFI framework. High-resolution TEM (HR-TEM) reveals distinct Fe_2O_3 nanoparticles anchored on the zeolite framework, evidenced by clear lattice fringes corresponding to the (110) and (104) planes (Fig. 1e and f). Furthermore, energy-dispersive X-ray spectroscopy (EDS) elemental maps (Fig. 1g) show a homogeneous distribution of the framework elements (Si, Al, and O), whereas Fe is concentrated in discrete locations, consistent with the presence of nanoparticles.

Atomic-resolution scanning transmission electron microscopy (AC-STEM) was used to probe the iron species in 0.1Fe@ZSM-5 at the atomic scale. The images (Fig. 1h–j and S3) revealed numerous distinct bright dots and ~1.5 nm particles, demonstrating that 0.1Fe@ZSM-5 is composed of both dispersed Fe atoms and nanoparticles (NPs). Electron energy loss spectroscopy (EELS) was subsequently conducted to analyze the oxidation state of the Fe species. The Fe L3 and L2 edges from three EELS line scans exhibited identical positions at 708.7 and 721.5 eV, respectively, consistent with the Fe^{3+} reference (Fig. 1k).[26] The combined results confirm the presence of small nanoparticles containing Fe^{3+} species on 0.1Fe@ZSM-5.

2.2 Coordination environment of Fe@ZSM-5

The physicochemical properties of the Fe@ZSM-5 catalysts were characterized by X-ray photoelectron spectroscopy (XPS), where the Fe 2p spectra varied significantly with iron loading (Fig. 2a). For samples with low iron content (0.05Fe@ZSM-5 and 0.08Fe@ZSM-5), distinct iron peaks were not resolved. In contrast, the 0.1Fe@ZSM-5 and 0.5Fe@ZSM-5 catalysts displayed well-defined peaks for Fe^{2+} ($2p_{3/2}$ at 710.8 eV) and Fe^{3+} ($2p_{3/2}$ and $2p_{1/2}$).[27–31] The presence of Fe^{3+} was further confirmed by satellite peaks at 718.8 eV and 733.0 eV.[32,33]

© 2025 The Author(s). Co-published by the Institute of Process Engineering, Chinese Academy of Sciences and the Royal Society of Chemistry

Open Access Article. Published on 15 December 2025. Downloaded on 2/5/2026 10:57:16 PM.
This article is licensed under a Creative Commons Attribution-NonCommercial 3.0 Unported Licence.

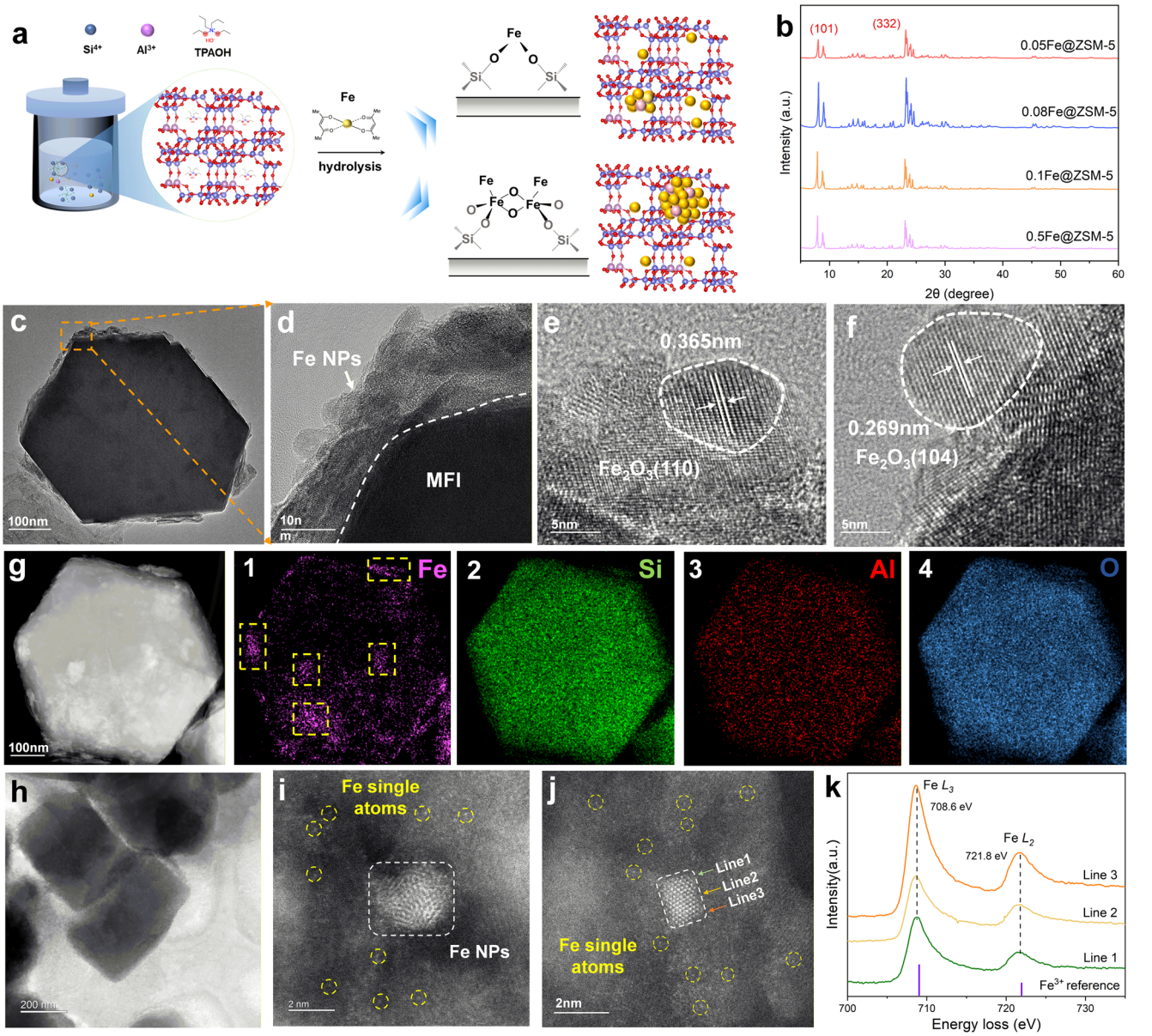

Fig. 1 Synthesis and structural characterization of Fe@ZSM-5 catalysts. (a) Schematic illustration of the synthesis of Fe@ZSM-5; (b) XRD patterns of the as-prepared Fe@ZSM-5 catalysts with different iron loadings; (c) TEM image of 0.5Fe@ZSM-5; (d–f) high-resolution TEM images of 0.5Fe@ZSM-5, showing Fe_2O_3 nanoparticles with resolved lattice fringes corresponding to the (110) and (104) planes; (g) HAADF-STEM image and the EDS elemental maps for Fe, Al, Si, and O in 0.5Fe@ZSM-5; (h–j) aberration-corrected STEM images of 0.1Fe@ZSM-5. Isolated single Fe atoms are marked by yellow circles, and Fe nanoclusters are highlighted by white squares; (k) Fe L-edge EELS spectra of 0.1Fe@ZSM-5.

Therefore, iron exists as a mixture of Fe^{2+} and Fe^{3+} in the higher-loading samples, with Fe^{3+} being the predominant species. The larger Fe^{3+} peak area for 0.5Fe@ZSM-5 is consistent with its higher total iron content.

The O 1s XPS spectra (Fig. 2b) were deconvoluted into three distinct components, corresponding to lattice oxygen ($O_{lattice}$) at a binding energy of 530.2 eV, surface-adsorbed oxygen ($O_{surface\text{-}adsorbed}$) at 531.7 eV, and adsorbed hydroxyl groups (O_{hydro}) at 532.6 eV.[34,35] It is worth noting that the parent HZSM-5 exhibits a large proportion of $O_{surface\text{-}adsorbed}$ which is associated with –Al/Si bonds.[36] While surface-adsorbed oxygen was the predominant species across all samples (49–54%) from parent HZSM-5 or metal oxides,[36–38] the concentration of lattice oxygen exhibited a notable, non-monotonic trend with increasing Fe content. For 0.1Fe@ZSM-5, it has the highest value of lattice oxygen of about 33.1%, and concurrently displayed the lowest concentration of adsorbed hydroxyl groups (14.9%). However, 0.5Fe@ZSM-5 shared the equivalent amount of lattice oxygen and adsorbed hydroxyl groups (both 20.7%). The variation suggests that moderate Fe incorporation promotes the generation of lattice oxygen while excessive Fe loading may bring hydroxyl enrichment, which enables the catalyst to obtain higher N_2 selectivity.

© 2025 The Author(s). Co-published by the Institute of Process Engineering, Chinese Academy of Sciences and the Royal Society of Chemistry

Open Access Article. Published on 15 December 2025. Downloaded on 2/5/2026 10:57:16 PM.
This article is licensed under a Creative Commons Attribution-NonCommercial 3.0 Unported Licence.

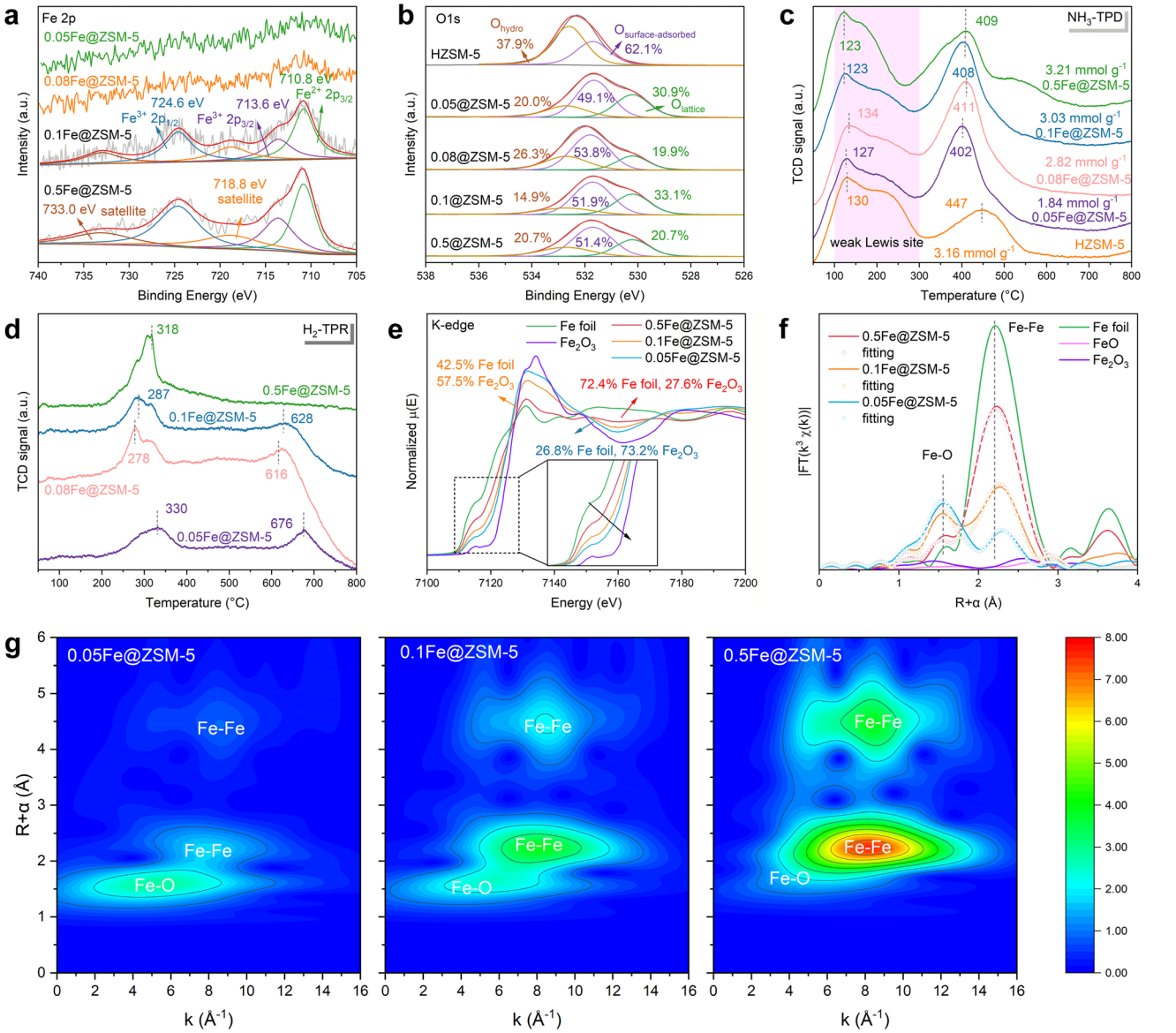

Fig. 2 Electronic state and coordination structure characterization on FeZSM-5. (a) Fe 2p spectra; (b) O 1s XPS spectra; (c) NH_3-TPD spectra; (d) H_2-TPR spectra; (e) K-edge XANES spectra; (f) K-edge EXAFS spectra; (g) Fe wavelet transforms. All FT and WT signals in this study are non-phase corrected.

The surface acidity of the Fe@ZSM-5 catalysts was further investigated using NH_3-TPD. As shown in Fig. 2c, the low-temperature peaks at 100–300 °C are ascribed to weak acid sites, corresponding to NH_3 release from the weaker Lewis acid sites associated with exchange metal ions.[39] Meanwhile, the high-temperature peaks at 400–500 °C correspond to strong acid sites exhibiting thermal stability.[39,40] Compared to HZSM-5, increasing the Fe loading shifts the high-temperature NH_3 desorption peak from 447 °C to approximately 410 °C, indicating a reconstruction in the acid site structure. The total quantified acidity for each Fe@ZSM-5 sample is about 3 mmol g^{-1}, comparable to that of HZSM-5. The surface acidity was detected by pyridine IR and the spectra (Fig. S4) reveal bands at 1450, 1545, 1625 and 1490 cm^{-1}, which are assigned to Lewis sites, Brønsted sites, and a combination of Lewis and Brønsted sites (B_{NH_4} + L_{NH_3} acid), respectively.[41] The quantitative analysis (Table S2) of Brønsted *vs.* Lewis (B/L) through pyridine-IR shows a marked decrease from 41.0 for HZSM-5 to 14.4–22.6 for Fe@ZSM-5, indicating a substantial reduction in Brønsted acidity and a relative increase in Lewis acidity upon Fe incorporation. Furthermore, the H_2-TPR profiles in Fig. 2d reveal the reducibility of Fe@ZSM-5. With increasing Fe loading, the initial peak corresponding to the reduction of Fe_2O_3 to Fe_3O_4 was intensified,[42] while the high-temperature region associated with the reduction of FeO particles to metallic Fe (Fe^{2+} to Fe^0) decreased in intensity.[43] This suggests that the Fe^{2+} observed in the XPS spectra may originate from the interaction between iron and the surrounding atoms.[44] The results also imply that Fe^{3+} predominates as the stable species at higher loadings.

© 2025 The Author(s). Co-published by the Institute of Process Engineering, Chinese Academy of Sciences and the Royal Society of Chemistry

Open Access Article. Published on 15 December 2025. Downloaded on 2/5/2026 10:57:16 PM.
This article is licensed under a Creative Commons Attribution-NonCommercial 3.0 Unported Licence.

X-ray absorption fine structure (XAFS) was employed to probe the coordination environment of iron within the synthesized Fe@ZSM-5 catalysts. The normalized Fe K-edge X-ray absorption near-edge structure (XANES) spectra are presented in Fig. 2e. The absorption threshold (E_0) for all samples is shifted to a higher energy relative to that of Fe foil, indicating that iron predominantly exists in an oxidized state.[45] As the iron loading decreases, the XANES spectra exhibit a further shift toward higher energy and a broadening of the normalized peak. These features are characteristic of the oxidation of Fe to Fe^{3+}, suggesting a higher average oxidation state in catalysts with lower iron content,[46] aligning with the fitting results in the XANES spectra.

The Fourier-transformed (FT) EXAFS spectra of the Fe@ZSM-5 catalysts (Fig. 2f) exhibit a prominent peak at ~2.5 Å, corresponding to the Fe–Fe scattering path. The intensity of this peak strengthens with increasing iron loading, while the intensity of the Fe–O scattering path at 1.8 Å concurrently diminishes. These trends indicate that higher iron loadings promote the formation of Fe nanoclusters. In contrast, lower loadings favor a coexistence of atomically dispersed Fe species and small nanoclusters. This structural model is corroborated by wavelet transform (WT) analysis (Fig. 2g), which clearly resolves the distinct scattering contributions from Fe–O and Fe–Fe paths. Quantitative EXAFS fitting provides further validation (Table S3). As the iron loading increases from 0.05 to 0.5 wt%, the Fe–Fe coordination number rises from 0.9 to 5.4, while the Fe–O coordination number decreases from 4.1 to 1.8. These results are in agreement with the structural evolution inferred from our XANES and WT analyses.

2.3 Dual kinetic effect of NH_3-SCR over Fe@ZSM-5

To identify the optimal support, we first evaluated the catalytic performance of the parent HZSM-5 zeolites with various Si/Al ratios (10, 27, 85, 130, and 240), as shown in Fig. 3a. The zeolite with a Si/Al ratio of 27 exhibited the highest activity. The catalytic performance of the Fe@ZSM-5 series in the SCR of NO with NH_3 was evaluated (Fig. 3b). By varying the Fe loading amount during ion exchange from 0.05 to 0.5 wt%, two distinct kinetic regimes were observed in catalytic tests over the 400–850 °C temperature range. In the low-temperature regime (400–700 °C), the NO conversion increased with both temperature and iron loading. The 0.5Fe@ZSM-5 catalyst achieved the highest performance, with an average NO conversion of 95.1%. In contrast, the parent HZSM-5 support showed poor activity (9.3–65.3% conversion), confirming that the iron species are the primary sites for activating NH_3-SCR, which improved the redox properties of the catalyst thereby accelerating the

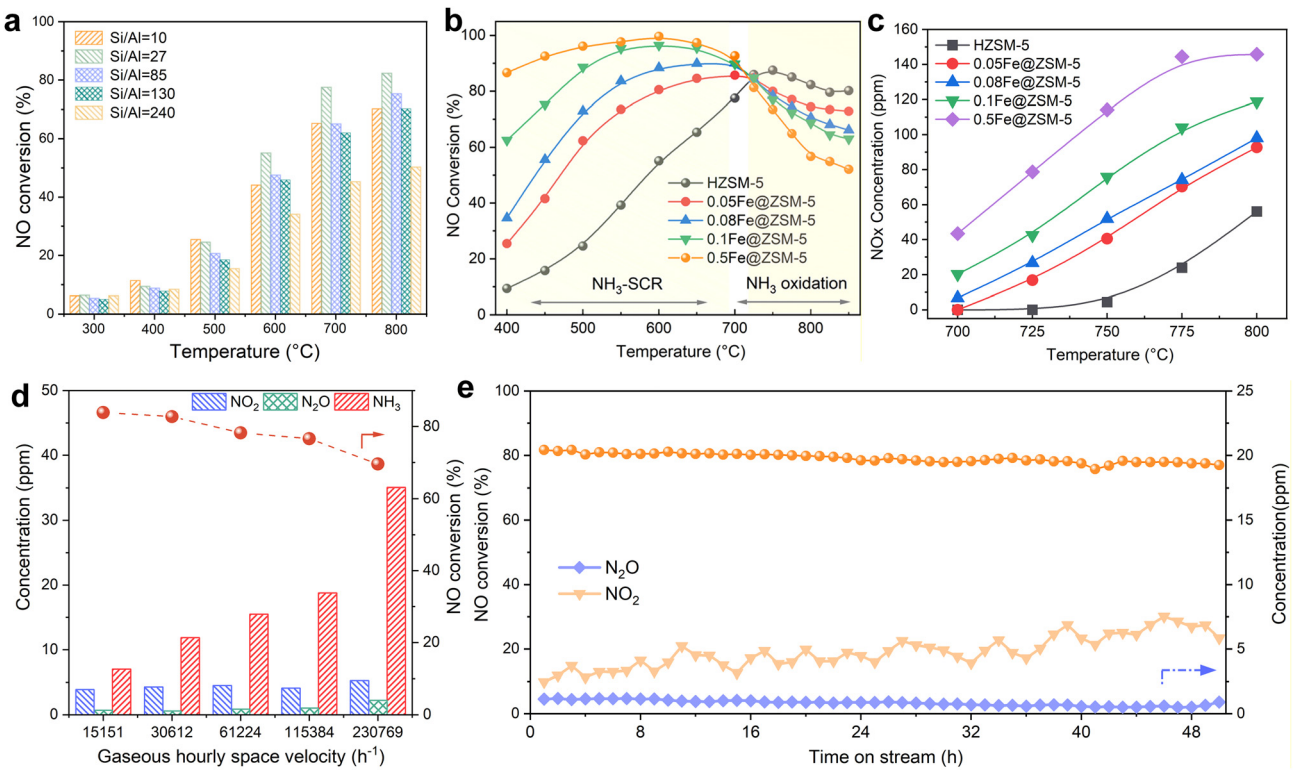

Fig. 3 NO catalytic reduction and NH_3 oxidation. NO conversion over (a) HSZM-5 with various Si/Al ratios and (b) Fe@ZSM-5 at different reaction temperatures; (c) effect of NO_x concentration on catalytic NH_3 oxidation at 700–850 °C; (d) effect of gas hourly space velocity on NO conversion; (e) time-on-line NO conversion and outlet concentration of N_2O and NO_2 over 0.1Fe@ZSM-5 at 700 °C. Conditions: 1000 ppm NH_3, 6.0 vol% O_2, 1000 ppm NO, and balance N_2.

© 2025 The Author(s). Co-published by the Institute of Process Engineering, Chinese Academy of Sciences and the Royal Society of Chemistry

Open Access Article. Published on 15 December 2025. Downloaded on 2/5/2026 10:57:16 PM.
This article is licensed under a Creative Commons Attribution-NonCommercial 3.0 Unported Licence.

reaction rates and catalytic performance.[47] However, at temperatures above 700 °C, this trend reversed. The NO conversion began to decrease with increasing temperature and iron loading, indicating a loss of activity and N_2 selectivity (Fig. S5).

To investigate this high-temperature inactivation, we performed separate catalytic oxidation of NH_3 in the presence of O_2. The concentration of NO_x produced from NH_3 oxidation increased with both temperature and iron loading (Fig. 3c). This result shows that at high temperatures, NH_3 oxidation becomes a dominant competing side reaction, consuming the reducing agent and thereby lowering the efficiency of NO reduction. Moreover, the lower NO concentration of pristine HZSM-5 further confirms this side reaction to the iron species. Combining the TEM and XAS results, we preliminary conclude that the iron nanoparticle size is an important factor in modulating the trade-off between NH_3-SCR activity and NH_3 oxidation.

The effect of gas hourly space velocity on the catalytic performance was explored (Fig. 3d). Increasing the space velocity led to a decrease in NO conversion. This was accompanied by a rise in unconverted NH_3 at the outlet, while the concentrations of NO_2 and N_2O by-products did not change significantly. These results indicate that the drop in NO conversion at higher space velocities is due to the reduced NH_3 conversion rather than the enhanced NH_3 over-oxidation.

In addition, the long-term stability of the 0.1Fe@ZSM-5 catalyst was tested at 700 °C (Fig. 3e). The catalyst demonstrated robust performance over a 50 hour run, with NO conversion showing only a slight decrease from 79.5% to 77.0%. During this period, the outlet NO_2 concentration increased from 4.1 to 7.5 ppm, while the N_2O concentration remained stable. This suggests that the minor drop in NO conversion is linked to a slow side reaction where some NO is oxidized to NO_2, which does not efficiently enter the fast SCR pathway.

Regarding practical application, we evaluated the long-term catalytic performance of synthesized 0.1Fe@ZSM-5 and HZSM-5 under exposure to 300 ppm SO_2 and 8.3

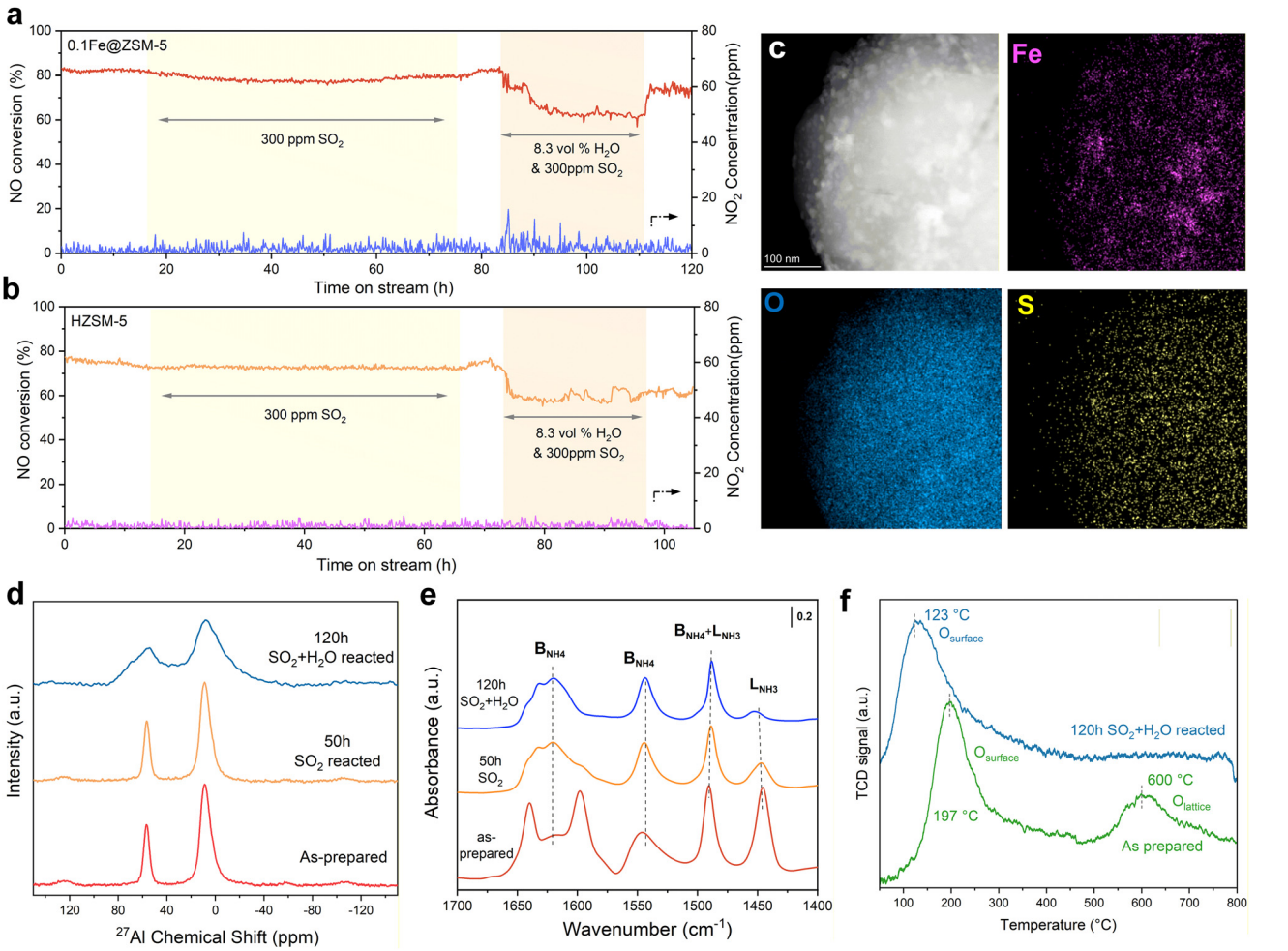

Fig. 4 The long-term stability test on synthesized (a) 0.1Fe@ZSM-5 and (b) HZSM-5 catalysts in the presence of SO_2 and H_2O; (c) magnified HAADF-STEM image and corresponding EDS maps of the reacted 0.1Fe@ZSM-5; (d) ^{27}Al MAS NMR spectra; (e) pyridine FTIR spectra; (f) O_2-TPD patterns of the as-prepared and reacted 0.1Fe@ZSM-5. Reaction conditions: 700 °C, 1000 ppm NH_3, 6.0 vol.% O_2, 1000 ppm NO, 300 ppm SO_2, 8.3 vol% H_2O and balance N_2 at a space velocity of 30 533 ml $g_{cat.}^{-1}$ h^{-1}.

© 2025 The Author(s). Co-published by the Institute of Process Engineering, Chinese Academy of Sciences and the Royal Society of Chemistry

Open Access Article. Published on 15 December 2025. Downloaded on 2/5/2026 10:57:16 PM. This article is licensed under a Creative Commons Attribution-NonCommercial 3.0 Unported Licence.

vol% H_2O at 700 °C. Under 300 ppm SO_2, 0.1Fe@ZSM-5 deactivated gradually, with NO conversion decreasing from 83.0% to 78.5% over 50 h as shown in Fig. 4a. Introducing 8.3 vol% H_2O accelerated deactivation and the conversion dropped to 60.1%. After both poisons were removed at 110 h, the catalyst partially recovered to 71.5%. For comparison, HZSM-5 showed a similar slight decline under SO_2 alone, from 77.3% to 72.1% NO conversion. With both SO_2 and H_2O, the conversion decreased to 60.8% and did not recover after poison removal, indicating irreversible deactivation.

Further physicochemical analyses were performed after 120 h continuous reaction to probe the deactivation mechanism of 0.1Fe@ZSM-5. HAADF-STEM and EDS reveal dispersed Fe nanoparticles. Sulfur deposits distribute broadly on ZSM-5 with partial co-localization on Fe nanoparticles, while remaining overall dispersed. The ^{27}Al MAS NMR spectra were used to track the evolution of the framework Al throughout the long-term hydrothermal ageing. As can be seen in Fig. 4d, the broad peak signal of dehydrated 0.1Fe@ZSM-5 is 4-coordinated corresponding to the Brønsted acidic Al(IV) site at 58 ppm. After SO_2 + H_2O ageing for 120 h, the signal intensity of the framework Al decreases, suggesting a dealumination process.[48] The significant decline of the L_{NH_3} peak from Py-IR clearly indicates the loss of Lewis acid sites after long-term poisoning (Fig. 4e). The O_2-TPD patterns (Fig. 4f) of the as-prepared catalyst and after 120 h in SO_2 and H_2O confirm a severe loss of lattice oxygen (over 400 °C)[49,50] and diminished oxygen mobility after exposure to SO_2 and H_2O.

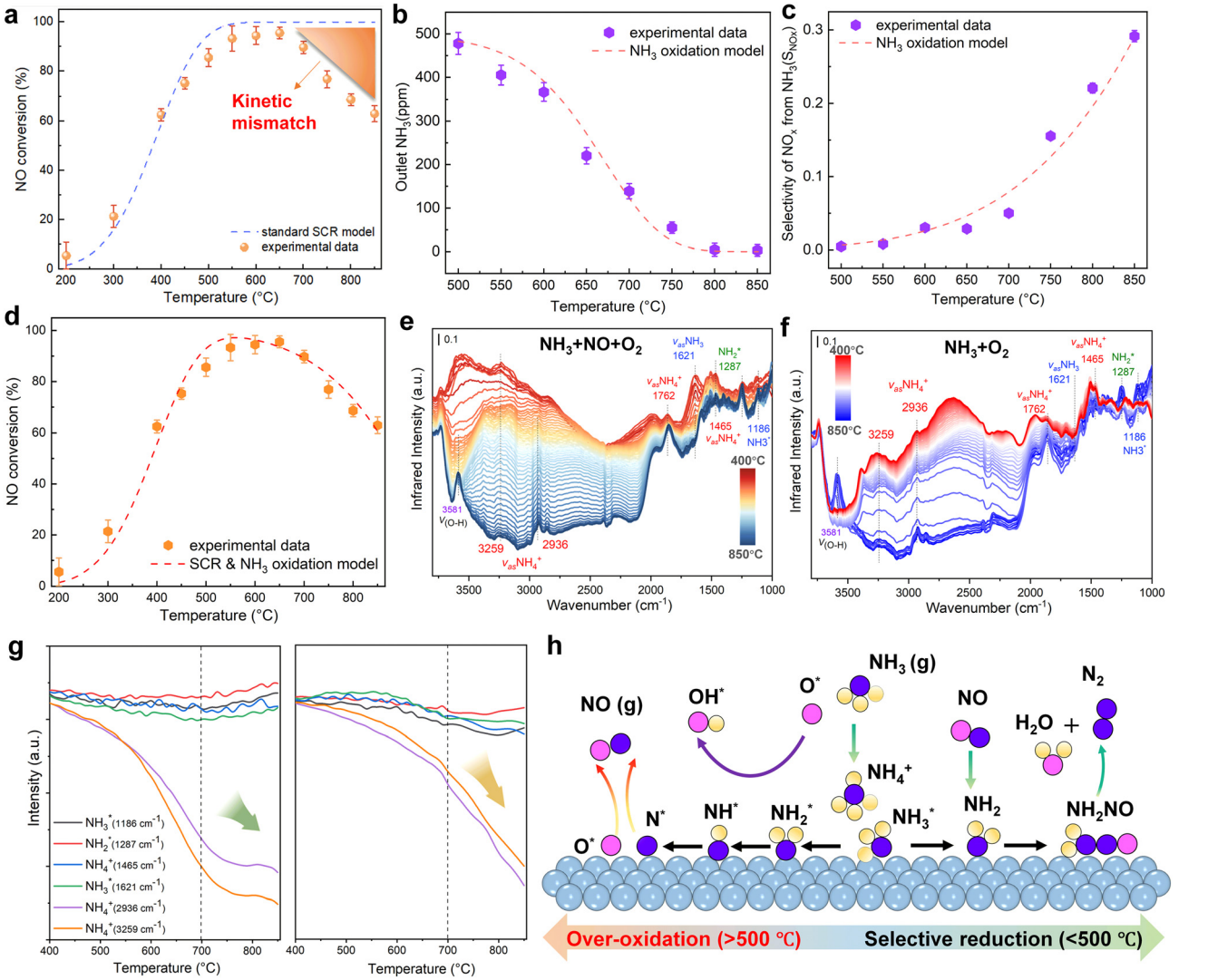

Fig. 5 Identification of the dual kinetic effect on 0.1Fe@ZSM-5. (a) Comparison of the conventional SCR kinetic model with experimental data under a NO + NH_3 + O_2 atmosphere; effect of reaction temperature on (b) NH_3 concentration and (c) NO_x selectivity under NH_3 + O_2 oxidation conditions; (d) comparison of the dual kinetic model and experimental data; *in situ* DRIFT spectra for (e) NO + NH_3 + O_2 reduction and (f) NH_3 + O_2 oxidation; (g) evolution of DRIFT spectra on intermediates; (h) schematic illustrating the proposed dual kinetic pathway for high-temperature SCR.

© 2025 The Author(s). Co-published by the Institute of Process Engineering, Chinese Academy of Sciences and the Royal Society of Chemistry

Open Access Article. Published on 15 December 2025. Downloaded on 2/5/2026 10:57:16 PM. This article is licensed under a Creative Commons Attribution-NonCommercial 3.0 Unported Licence.

These observations indicate that sulfur deposition blocks active oxygen sites and suppresses lattice oxygen participation in the long-term test.

2.4 Kinetics of NO reduction and NH_3 oxidation

Catalytic experiments revealed that NH_3 oxidation significantly influences the overall reaction kinetics at high temperatures, with its rate being dependent on the Fe loading. Consequently, a conventional kinetic model for standard SCR fails to accurately describe the system at 700 °C (Fig. 5a). We therefore developed a dual-pathway kinetic model that considers both the NH_3 oxidation and NO reduction reactions. The model parameters, governing equations, and diffusion criteria are detailed in the SI.

Under NH_3 + O_2 atmospheric conditions, NH_3 oxidation products on the catalyst surface can be primarily classified as N_2 and NO, with selectivity varying as the temperature increases. Higher temperatures favor higher NO selectivity.

$$4NH_3 + 3O_2 \rightarrow 2N_2 + 6H_2O \quad (1)$$

$$4NH_3 + 5O_2 \rightarrow 4NO + 6H_2O \quad (2)$$

The NO generation rate due to NH_3 oxidation, $S_{NH_3\text{–}NO}$, is considered as shown

$$\frac{dC_{NH_3}}{dt} = -\rho_{catal} S_{catal} \eta_{NH_3} k_{NH_3} \theta_{NH_3} C_{O_2} \quad (3)$$

$$S_{NH_3\text{–}NO} = \frac{k_{NH_3\text{–}NO}\theta_{NH_3} C_{O_2}}{k_{NH_3\text{–}NO}\theta_{NH_3} C_{O_2} + k_{NH_3\text{–}N_2}\theta_{NH_3} C_{O_2}} \quad (4)$$

$$\frac{dC_{NO}}{dt} = -\frac{dC_{NH_3}}{dt} S_{NH_3\text{–}NO} = -\frac{dC_{NH_3}}{dt} \frac{k_{NH_3\text{–}NO}}{k_{NH_3\text{–}NO} + k_{NH_3\text{–}N_2}} \quad (5)$$

Experimental measurement data under NH_3 + O_2 conditions were analyzed by selecting data points where NH_3 conversion remained below 15% to minimize diffusion effects on fitting accuracy. Here, $\theta_{NH_3} = \frac{k_{ad} C_{NH_3}}{k_{ad} C_{NH_3} + 1}$ represents the NH_3 surface coverage. After optimization, the rate constants for NH_3 oxidation reactions at various temperatures yielded an activation energy of 98.3 kJ mol^{-1}. The pre-exponential factor A and activation energy E_a for the NH_3 oxidation process were subsequently determined by fitting the $\ln k_x$ *vs.* $1/T$ relationship according to the Arrhenius equation. We compare the experimental measurements and model calculations for NH_3 conversion and NH_3-to-NO oxidation selectivity under NH_3 + O_2 atmospheric conditions. The calculated results demonstrate good agreement with experimental data over the 500–850 °C temperature range (Fig. 5b and c).

Under NH_3 + NO + O_2 atmospheric conditions, the reaction rate of NO is governed by the synergistic interplay between the catalytic reduction of NO by NH_3 and the concurrent catalytic oxidation of NH_3 to form NO. This dual mechanism significantly influences the overall reaction kinetics, as demonstrated below:

$$4NO + 4NH_3 + O_2 \rightarrow 4N_2 + 6H_2O \quad (6)$$

$$4NH_3 + 3O_2 \rightarrow 2N_2 + 6H_2O \quad (7)$$

$$4NH_3 + 5O_2 \rightarrow 4NO + 6H_2O \quad (8)$$

The NO reaction rate can be expressed by the following equation:

$$\frac{dC_{NH_3}}{dt} = -\rho_{catal} S_{catal} \eta_{NH_3} k_{NH_3} \theta_{NH_3} C_{O_2} \quad (9)$$

$$\frac{dC_{NO}}{dt} = -\rho_{catal} S_{catal} \eta_{NO} k_{re} \theta_{NH_3} C_{NO} + \frac{dC_{NH_3}}{dt} S_{NH_3\text{–}NO} \quad (10)$$

Subsequently, the experimental data obtained under NH_3 + NO + O_2 conditions were systematically analyzed. Given the relatively low SNCR efficiency observed below 850 °C, gas-phase NH_3 + NO + O_2 reactions were excluded from consideration in this temperature range. To minimize the influence of mass transfer limitations on fitting accuracy, experimental data points with NO conversion rates below 15% were specifically selected for kinetic analysis. Through optimization procedures, the rate constants for NO catalytic reduction reactions were determined at various temperatures. The pre-exponential factor (A) and activation energy (E_a) for the NH_3 oxidation process were subsequently derived by fitting the $\ln(k_x)$ *versus* $1/T$ relationship according to the Arrhenius equation, as presented in Table S4.

Compared to conventional SCR kinetic models, this work introduces a dual kinetic framework that explicitly incorporates NH_3 surface oxidation as a competing reaction under high-temperature conditions. A key feature of this framework is the inclusion of the selectivity of NH_3 toward NO formation as a temperature-dependent parameter, which allows quantitative evaluation of how the NH_3 over-oxidation pathway influences the overall SCR performance. This integration provides a more accurate description of the experimental results (Fig. 5d). As the temperature rises, the model successfully captures the transition where the NO formation rate surpasses the N_2 formation rate, revealing the increasing contribution of NH_3 oxidation in determining overall selectivity. By incorporating this temperature-dependent selectivity, the dual kinetic model addresses a gap in prior SCR kinetic frameworks, which typically treat NH_3 oxidation as a parallel but independent side reaction.

To explore the effect of NH_3 catalytic oxidation on SCR-related intermediates, *in situ* DRIFT measurements combined with TPSR were performed on 0.1Fe@ZSM-5 from 400 to 850 °C (Fig. 5e). Following NH_3 adsorption, broad N–H vibration peaks at 3259 and 2936 cm^{-1} are ascribed to

© 2025 The Author(s). Co-published by the Institute of Process Engineering, Chinese Academy of Sciences and the Royal Society of Chemistry

Open Access Article. Published on 15 December 2025. Downloaded on 2/5/2026 10:57:16 PM.
This article is licensed under a Creative Commons Attribution-NonCommercial 3.0 Unported Licence.

the asymmetric stretching as $\nu_{as}(NH_4^+)$ on Brønsted acid sites, where three hydrogen atoms bond to oxygen ions in the AlO_4 tetrahedra.[51,52] The sharp peaks at 3581 and 3660 cm^{-1} are attributed to Si–OH–Al and Si–OH, respectively. In the lower wavenumber region, the peak at 1287 cm^{-1} corresponds to NH_2^* vibrations, while features at 1186 and 1621 cm^{-1} are assigned to $\nu_{as}(NH_3)$ on Lewis acid sites, and those at 1465 and 1762 cm^{-1} to NH_4^+ vibrations on Brønsted acid sites.[53] Upon heating in an NH_3–NO–O_2 atmosphere to 600 °C, the intensities of NH_3^* and NH_4^+ intermediates at 3259 and 1621 cm^{-1} decay rapidly, whereas NH_2^* remains relatively stable, indicating that certain NH_3^* and NH_4^+ species serve as the initial active sites in the SCR redox cycle during activation. Notably, as the temperature further increased from 600 to 850 °C, only the absorbance of NH_4^+ intermediates at 3259 and 2936 cm^{-1} decreased significantly, whereas the band at 1465 cm^{-1} remained relatively stable. This observation indicates that framework Brønsted acid sites participate more actively in the synergistic conversion of NH_3 and NO at high temperatures. Moreover, the time-resolved DRIFT spectra of 0.1Fe@ZSM-5 during NH_3 adsorption, O_2 oxidation, and NO reduction at 800 °C (Fig. S6–S8) confirm the dynamic transformation of NH_4^+ species during the redox cycle.

For comparison, variations in intermediates during exposure to an NH_3 + O_2 atmosphere at 400–850 °C were also examined under NH_3 catalytic oxidation conditions (Fig. 5f). At 400 °C, the NH_2^* intermediate at 1287 cm^{-1} is markedly lower than that in NH_3 + NO + O_2, but its intensity reverses and increases upon heating to 800 °C, confirming that dehydrogenation products of NH_3 or NH_4^+ proceed *via* the NH_2^* pathway in high-temperature oxidizing environments, while NH_3^* remains relatively inert. For quantitative comparison, normalized absorbance changes of characteristic peaks with temperature are shown in Fig. 5g, suggesting that NH_4^+ likely participates in surface species consumption during NH_3 oxidation. Drawing from these observations, we propose a molecular-level pathway governed by a dual kinetic regime (Fig. 5h). Under moderate temperature conditions, a favorable activation barrier promotes the dehydrogenation of NH_3 to form NH_2^* intermediates. These species subsequently undergo N–N coupling to yield NH_2NO^*, which decomposes into N_2 following the conventional SCR pathway. Conversely, at temperatures exceeding 700 °C, the higher thermal energy shifts the reaction toward an undesirable oxidation route. In this regime, lattice oxygen induces the progressive dehydrogenation of adsorbed NH_3 at acid sites through sequential N–H bond scission. This process generates highly reactive NH* or N* radicals that are ultimately oxidized to NO_x.

To probe the influence of the iron nanoparticle size on the SCR mechanism, we performed *in situ* DRIFT experiments on the 0.05Fe@ZSM-5, 0.08Fe@ZSM-5, and 0.5Fe@ZSM-5 catalysts. Following NH_3 adsorption at 200 °C (Fig. 6a–c), distinct changes in the DRIFT spectra were observed as the Fe loading increased from 0.05 to 0.5 wt%. Correlating with the XANES fitting results, which indicated increasing metallic Fe content at higher loadings, these spectral changes suggest that metallic Fe influences the NH_3 adsorption behavior. Specifically, the

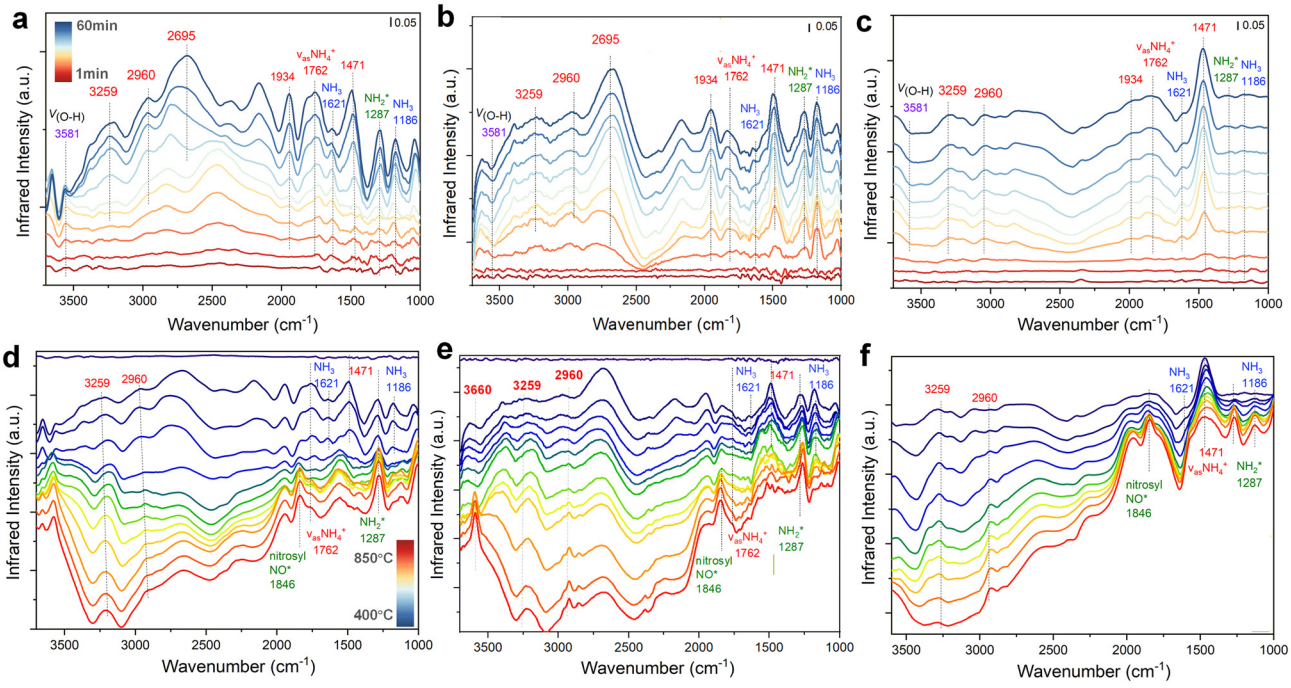

Fig. 6 Effect of iron nanoparticles on the high-temperature SCR mechanism. *In situ* DRIFT spectra of NH_3 adsorption at 200 °C on (a) 0.05Fe@ZSM-5, (b) 0.08Fe@ZSM-5, and (c) 0.5Fe@ZSM-5; TPSR on (d) 0.05Fe@ZSM-5, (e) 0.08Fe@ZSM-5, and (f) 0.5Fe@ZSM-5 at 400 to 850 °C.

© 2025 The Author(s). Co-published by the Institute of Process Engineering, Chinese Academy of Sciences and the Royal Society of Chemistry

Open Access Article. Published on 15 December 2025. Downloaded on 2/5/2026 10:57:16 PM. This article is licensed under a Creative Commons Attribution-NonCommercial 3.0 Unported Licence.

intensity of the band corresponding to NH_3 coordinated to Lewis acid sites decreased, while the band assigned to NH_4^+ ions at 1471 cm^{-1} grew substantially. This shift indicates that NH_3 preferentially adsorbs at Brønsted acid sites in the presence of metallic Fe species, where it forms more stable NH_4^+ species. The enhanced stability at Brønsted sites suppresses the excessive oxidation of NH_3 at high temperatures, thereby improving the selectivity toward N_2 formation.[54] Furthermore, the band at 3259 cm^{-1}, attributed to NH_4^+ ions interacting with Brønsted acid sites of the zeolite, was attenuated, indicating a weaker interaction between the agglomerated iron species and the zeolite framework.

As the temperature was increased (Fig. 6d–f), the intensity of all ammonia-related bands decreased, indicating the progressive desorption of NH_3 from the acid sites. Notably, the evolution of the surface species differed significantly with iron loading. For the low-loading 0.05Fe@ZSM-5 and 0.08Fe@ZSM-5 catalysts, the bands for NH_3 adsorbed on Lewis acid sites were almost completely consumed by 700–850 °C, whereas the signals for NH_4^+ and NH_2^* species persisted. This suggests that the latter are more thermally stable and likely serve as key intermediates in the redox reaction. In contrast, for the 0.5Fe@ZSM-5 catalyst, the bands corresponding to nitrosyl species at 1846 cm^{-1} were significantly more intense.[55] Concurrently, the consumption of the NH_4^+ band at 3259 cm^{-1} was more pronounced, indicating that the larger iron nanoparticles promote the undesirable over-oxidation of ammonia to NO at high temperatures, which is in agreement with the observed SCR performance.

3 Conclusions

In summary, we have developed a sinter-resistant 0.1Fe@ZSM-5 catalyst whose exceptional stability in high-temperature NH_3-SCR is attributed to the confinement of ultrasmall Fe nanoclusters within the zeolite framework. Its structural integrity was confirmed, with minor long-term deactivation resulting from sulfur deposition rather than framework collapse or Fe sintering. Through a combination of *in situ* DRIFTS and kinetic analysis, we have established a dual-pathway mechanism that accurately captures the transition from the conventional NO-reduction route to the high-temperature NH_3-oxidation-dominated regime. Unlike traditional SCR kinetic models, which assume independent or single-pathway behavior, the dual-pathway model explicitly incorporates the competing oxidation of NH_3 by treating the selectivity of NH_3 toward NO formation as a temperature-dependent parameter. This approach reveals how the interplay between NH_3 consumption by oxidation and its availability for SCR modifies apparent activation energies and selectivity trends, providing improved predictive capability across the entire temperature range. These studies identified the distinct roles of key surface intermediates, providing direct evidence for NH_2^* as a critical species in the NO reduction pathway, which competes with the NH_3 oxidation route. These findings offer a new strategy for the rational design of robust catalysts for challenging industrial applications. The development of a stable catalyst structure, coupled with a more accurate kinetic model, paves the way for advancing high-performance deNO_x technologies to meet stringent emission regulations.

4 Experimental and computational section

4.1 Catalyst synthesis and activity measurement

The HZSM-5 zeolite was prepared *via* a hydrothermal synthesis route. A precursor gel was formed by dissolving ethylenediamine (EDA, 1.20 g), tetraethyl orthosilicate (TEOS, 8.32 g), NaOH (0.3 g), and $NaAlO_2$ (1.02 g) in an aqueous solution containing distilled water (15 g) and the structure-directing agent (SDA), tetramethylammonium hydroxide ($TMADa^+$, 13 g). After stirring for 6 h at room temperature, the gel was transferred to a 100 mL Teflon-lined autoclave and crystallized at 170 °C for 3 days. The resulting solid product was calcined at 800 °C for 5 h (with a heating ramp of 5 °C min^{-1}) to remove the SDA. To produce the final parent material, the calcined powder was ion-exchanged by washing three times with a 0.2 M NH_4NO_3 solution at 70 °C, followed by drying at 110 °C for 12 h.

For the fabrication of Fe@ZSM-5, a suspension was created by mixing 10 g of HZSM-5 in 100 ml of distilled water, under intense stirring. The necessary quantity of iron acetylacetonate ($Fe(C_5H_7O_2)_3$) was dissolved in this mixture. Ensuing continuous magnetic agitation at 80 °C for 3 h facilitated the homogenization of the solution, which was then subjected to filtration and thrice rinsed with distilled water. The filtrate was air-dried at 110 °C for 12 h, followed by calcination in a muffle furnace at 800 °C for 5 h under ambient air conditions. The resultant catalyst particles were sieved to obtain a granule size range between 0.18 and 0.25 mm.

The catalytic performance for the NH_3-SCR of NO_x was evaluated in a continuous-flow quartz fixed-bed reactor over a temperature range of 400–850 °C. The standard feed gas consisted of 1000 ppm NH_3, 1000 ppm NO, and 6 vol% O_2, with N_2 as the balance gas. The total flow rate was maintained at 2 L min^{-1} using mass flow controllers, corresponding to a gas hourly space velocity (GHSV) of 30 000 h^{-1}. The effluent gas concentrations (NO, NH_3, N_2O, NO_2, and O_2) were continuously monitored using an online infrared (IR) gas analyzer. To comprehensively assess the catalyst, several experiments were conducted: (i) the effect of GHSV on NO reduction was systematically investigated; (ii) long-term stability tests were performed under standard reaction conditions; (iii) the catalyst's resistance to poisoning was evaluated in the presence of 300 ppm SO_2 and/or 8.3 vol% H_2O. Prior to data acquisition for each point, the system was allowed to reach a steady state, and the reported values represent the average of

© 2025 The Author(s). Co-published by the Institute of Process Engineering, Chinese Academy of Sciences and the Royal Society of Chemistry

Open Access Article. Published on 15 December 2025. Downloaded on 2/5/2026 10:57:16 PM. This article is licensed under a Creative Commons Attribution-NonCommercial 3.0 Unported Licence.

measurements taken over a 20 minute period. The NO reduction efficiency, N_2 selectivity, and apparent reaction kinetics were calculated using the following equations:

$$X_{NO} = \left(\frac{[NO]_{inlet} - [NO]_{outlet}}{[NO]_{inlet}}\right) \times 100\% \quad (11)$$

$$N_2 \text{ selectivity } (\%) = \left(1 - \frac{[NO_2]_{outlet} + 2[N_2O]_{outlet}}{[NH_3]_{inlet} + [NO]_{inlet} - [NH_3]_{outlet} - [NO]_{outlet}}\right) \times 100\% \quad (12)$$

$$k\left[\text{mol g s}^{-1}\right] = \frac{X_{NO}[\%] \times F_{NO}\left[\text{L min}^{-1}\right]}{m[g] \times 60\left[\text{s min}^{-1}\right] \times 22.4\left[\text{L min}^{-1}\right] \times 100} \quad (13)$$

where X_{NO} denotes the conversion efficiency of NO, k represents the catalyst's reaction rate, F_{NO} is the initial flow rate of NO through the system, and m indicates the mass of the catalyst utilized.

4.2 Characterization and computational methods

The loading of Fe was determined by inductively coupled plasma (ICP, Agilent ICP-OES 725 ES). The crystallinity was assessed by X-ray diffraction (XRD) using a D8 Advance instrument with a scanning angle range (2-theta) from 5° to 90°. X-ray photoelectron spectroscopy (XPS) was conducted on a Thermo Scientific Nexsa. The obtained binding energy was externally calibrated by the carbonaceous C 1s of 284.6 eV. Surface areas and pore size distributions were quantified *via* the Brunauer–Emmett–Teller (BET) analysis and Barrett–Joyner–Halenda (BJH) method, determined by N_2 physisorption performed on an ASAP 2460 (Micromeritics) by degassing at 150 °C for 8 h. The morphologies were investigated using scanning electron microscopy (SEM) and scanning-transmission electron microscopy (STEM) *via* an FEI, Tecnai F20. Electron energy loss spectroscopy (EELS) was conducted with a Gatan Model 977 Enfinium ER EELS spectrometer. *In situ* infrared spectroscopy and diffuse reflectance UV-vis spectroscopy (UV-3600i Plus, Shimadzu) were employed to explore the dynamics of the catalytic processes. Nuclear magnetic resonance (NMR, Bruker 400 M) and K-edge X-ray absorption fine structure (XAFS) analyses were performed with Si (111) crystal monochromators at the BL14W beam line at the Shanghai Synchrotron Radiation Facility (SSRF) (Shanghai, China). Before the analysis at the beamline, samples were placed into aluminum sample holders and sealed using Kapton tape film. The XAFS spectra were recorded at room temperature using a 4-channel silicon drift detector (SDD) Bruker 5040. The obtained spectra were refined and analyzed using Athena. Athena and Artemis software programs were employed to perform the EXAFS fitting.[56] The software developed by Funke and Chukalina was applied to execute wavelet transformation using the Morlet wavelet with κ = 5 and σ = 1.[57]

Hydrogen temperature-programmed reduction (H_2-TPR) was conducted on an AutoChem II 2920 instrument to evaluate the reducibility of the catalysts. In a typical measurement, 100 mg of the sample was loaded into a U-shaped quartz tube. The catalyst was pretreated at 300 °C for 1 h under a flowing He atmosphere (heated at 10 °C min^{-1}) to remove adsorbed water. After the sample was cooled to 50 °C, the gas flow was switched to a 10 vol% H_2/He mixture (30 mL min^{-1}). The temperature was then ramped to 800 °C at a rate of 10 °C min^{-1}, and H_2 consumption was continuously monitored with a thermal conductivity detector (TCD).

The acidic properties of the catalysts were characterized by ammonia temperature-programmed desorption (NH_3-TPD) and oxygen storage and mobility were evaluated by oxygen temperature-programmed desorption (O_2-TPD) using the same instrument. Prior to the analysis, 100 mg of the sample was pretreated in a He flow at 300 °C for 1 h (10 °C min^{-1} ramp) and cooled to 50 °C. For NH_3-TPD, the sample was saturated with ammonia by exposure to a 10% NH_3/Ar stream (25 mL min^{-1}) for 1 h, followed by Ar purging for 1 h to remove physisorbed ammonia, and then heated to 800 °C at a rate of 10 °C min^{-1}, monitoring the amount of desorbed NH_3 using the TCD. In O_2-TPD, oxygen saturation was achieved by exposing the pretreated sample to 10% O_2/He (25 mL min^{-1}) for 1 h, followed by Ar purging for 1 h and subsequent heating to 800 °C at 10 °C min^{-1}.

4.3 Reaction kinetics modeling

For the fixed bed reactor, the following assumptions were made: 1. negligible volumetric flow changes along the catalyst bed, maintaining consistency throughout the reaction section; 2. negligible pressure variations before and after the catalyst bed, *i.e.*, no pressure drop; 3. negligible radial and axial diffusion, maintaining uniform gas concentration at the interface. These assumptions simplified the model to a one-dimensional plug flow reaction process, establishing the conservation equation for gas component x:

$$\frac{\partial C_x}{\partial t} + u\frac{\partial C_x}{\partial z} = r_x \quad (14)$$

where u represents the main gas flow linear velocity (m s^{-1}), and r_x represents the reaction rate of component x (mol m^{-3} s^{-1}). The corresponding boundary conditions are:

$$\begin{cases} z = 0,\ C_x = C_{x,\text{inlet}} \\ z = h,\ C_x = C_{x,\text{outlet}} \end{cases} \quad (15)$$

The catalyst bed thickness is h, C_x represents the component concentration of reactants/products (mol m^{-3}), primarily C_{NH_3}, C_{NO}, and C_{O_2} in this study, and k_x (mol m^{-2} s^{-1}) represents the reaction rate constant for each component. Subsequently, the rate equation was established:

$$r_x = k_x f(C_x) \quad (16)$$

© 2025 The Author(s). Co-published by the Institute of Process Engineering, Chinese Academy of Sciences and the Royal Society of Chemistry

Open Access Article. Published on 15 December 2025. Downloaded on 2/5/2026 10:57:16 PM. This article is licensed under a Creative Commons Attribution-NonCommercial 3.0 Unported Licence.

Specifically, for the NH_3 + O_2 catalytic oxidation process on 0.1Fe@ZSM-5, NH_3 adsorption based on the Langmuir model and O_2 effects were primarily considered.[58] For the comprehensive NH_3 + NO + O_2 reaction process, referring to standard SCR kinetic models, the reaction orders for NH_3, NO, and O_2 are 0, 1, and 0.5, respectively.[59] The O_2 content in coal combustion flue gas is approximately 6 vol%, with concentrations being orders of magnitude higher than other reaction gases, allowing neglect of concentration changes due to reaction during calculations. Additionally, according to the Mear criterion, since the external diffusion rate of catalyst particles is much lower than the reaction rate, diffusion effects on the gas–solid reaction process in this study can be neglected.[60]

Considering the influence of reactant gas internal diffusion within catalyst particles, an effectiveness factor η was introduced:

$$\eta = \frac{2}{\phi_1}(\phi_1 \coth \phi_1 - 1) \tag{17}$$

The Thiele modulus expression is given as $\phi_1 = R\sqrt{\frac{k_x}{D_{x,\mathrm{eff}}}}$, where R represents the catalyst particle diameter (m). For molecular sieve catalysts with porous structure characteristics, the comprehensive diffusion coefficient $D_{x,\mathrm{eff}}$ (m^2 s^{-1}) of gas component x is not only influenced by molecular diffusion and Knudsen diffusion (assuming a zeolite pore diameter of 10 nm) but also requires porosity correction. For the catalytic NO_x reduction reaction, the effectiveness factor ϕ_n approaches 1, indicating that the entire process is under surface reaction control. Other model-related parameter values are shown in Table S5.

$$D_{x,\mathrm{eff}} = \varepsilon^2 D_x \tag{18}$$

Here, $D_{x,\mathrm{gas}}$ represents the diffusion coefficient of reaction gases in air. For NH_3, the Fuller equation yields a calculated value of 0.198 cm^2 s^{-1} under standard conditions, while the diffusion coefficient of NO molecules in air is 0.168 cm^2 s^{-1} (with temperature corrections applied as needed). In actual reaction processes, gas–solid reactions compete with intraparticle diffusion $D_{x,\mathrm{KA}} = \frac{d_{\mathrm{pore}}}{3}\sqrt{\frac{8k_{\mathrm{B}}NT}{\pi M}}$. The combined effects of intraparticle diffusion and the chemical reaction on the overall reaction rate can be determined through the effectiveness factor and Thiele modulus.

4.4 *In situ* DRIFT measurement

In situ DRIFT spectroscopic analysis was conducted using a NICOLET iS50 FTIR spectrometer. Diffuse reflectance infrared Fourier transform spectra (DRIFTS) were acquired with a Harrick Praying Mantis attachment (Model DRK-4, featuring a water-cooling circulation system). Ambient diffuse reflectance UV-vis spectroscopy was performed on a Cary 400 spectrometer (Varian) outfitted with a diffuse reflectance unit. These UV-vis and DRIFTS examinations are pivotal for elucidating the nature of transient species in the *in situ* SCR process, thereby enhancing our comprehension of the reaction dynamics. To optimize detector performance, specifically the mercury cadmium telluride (MCT/A) detector, liquid nitrogen was utilized to regulate its operational temperature. The temperature within the experimental chamber was managed using a Harrick temperature control unit (Model ATC-024-2), complemented with a water-cooling system to mitigate potential overheating. Prior to initiating measurements, background spectra were obtained using the prepared samples. Subsequently, the catalyst was evenly distributed within the Harrick chamber. A mixture of reaction gases (NH_3/NO/O_2/He) was precisely regulated using mass flow controllers (MFCs) and warmed before being introduced into the chamber, with an overall gas flow rate set at 50 mL min^{-1}.

The procedure for conducting *in situ* UV-vis and DRIFTS analyses comprised the following steps: (1) NH_3 adsorption: the chamber was purged with He at 500 °C for 1 h and then brought back to ambient temperature. Subsequently, a flow of 1000 ppm NH_3/He was introduced, gradually elevating the temperature from 100 to 800 °C at 10 °C min^{-1}. (2) NH_3 oxidation: upon reaching adsorption equilibrium (typically within 1 h) at a set temperature, 6 vol% O_2 was infused into the chamber for 30 min. (3) NH_3–NO–O_2 co-presence and pulse: following equilibrium establishment (usually within 30 min) at the required temperature, a mixture of 1000 ppm NO, 6 vol% O_2, and 1000 ppm NH_3 in He was simultaneously fed into the chamber at 800 °C. For pulse tests, specific gas components were selectively discontinued. For the temperature programmed surface reaction (TPSR), the reaction chamber was heated from 400 °C to 850 °C in 1000 ppm NO and 6 vol% O_2 after exposure to 1000 ppm NH_3/He for 1 h. *In situ* DRIFT spectra were recorded every 8 seconds, and the IR spectrum presented subsequently represents the average interference pattern across eight successive scans.

The acidity of the samples was determined by pyridine infrared spectroscopy (Py-IR) on a Bruker Vector 22 spectrophotometer. Prior to the tests, the samples were shaped into tablets and degassed under vacuum at 400 °C for 1 h. After cooling to room temperature (RT), the samples were saturated with pyridine and then desorbed at RT, 200, and 450 °C under vacuum for 30 min. The IR spectra were registered in the 1400–1700 cm^{-1} range.

Author contributions

Xinlin Xie: investigation, software, writing – original draft. Jibin Yuan: data curation, methodology, writing – original draft. Lei Liu: methodology, writing – review & editing. Hanzi Liu: investigation, methodology, conceptualization, data curation, formal analysis, writing – original draft. Zhiqiang Sun: supervision, project administration, funding acquisition, writing – review & editing.

© 2025 The Author(s). Co-published by the Institute of Process Engineering, Chinese Academy of Sciences and the Royal Society of Chemistry

Open Access Article. Published on 15 December 2025. Downloaded on 2/5/2026 10:57:16 PM. This article is licensed under a Creative Commons Attribution-NonCommercial 3.0 Unported Licence.

Conflicts of interest

The authors declare no conflicts of interest.

Data availability

The data that support the findings of this study are available from the corresponding author upon reasonable request.

Supplementary information (SI): containing additional performance and structural data, as well as *in situ* DRIFTS. See DOI: https://doi.org/10.1039/d5im00245a.

Acknowledgements

We acknowledge the National Natural Science Foundation of China (52306179) and the Provincial Natural Science Foundation of Hunan (2024JJ6507).

References

1 L. Han, S. Cai, M. Gao, J.-Y. Hasegawa, P. Wang, J. Zhang, L. Shi and D. Zhang, Selective catalytic reduction of NO_x with NH_3 by using novel catalysts: State of the art and future prospects, *Chem. Rev.*, 2019, **119**, 10916–10976.

2 Y. Qu, G. Xu, C. Chen, J. Guo, D. Liu, H. Jia, H. Guo, S. Jia, J. Jia, Y. Zhang and L. Yan, A guideline to optimizing the performance of V_2O_5-MoO_3/TiO_2 catalysts for low-temperature SCR denitrification in industrial application, *Ind. Chem. Mater.*, 2025, DOI: 10.1039/D5IM00055F.

3 S. Y. Joshi, A. Kumar, J. Luo, K. Kamasamudram, N. W. Currier and A. Yezerets, New insights into the mechanism of NH_3-SCR over Cu- and Fe-zeolite catalyst: Apparent negative activation energy at high temperature and catalyst unit design consequences, *Appl. Catal., A*, 2018, **226**, 565–574.

4 M. Liu, C. Miao and Z. Wu, Recent advances in the synthesis, characterization, and catalytic consequence of metal species confined within zeolite for hydrogen-related reactions, *Ind. Chem. Mater.*, 2024, **2**, 57–84.

5 S. J. Schmieg, S. H. Oh, C. H. Kim, D. B. Brown, J. H. Lee, C. H. F. Peden and D. H. Kim, Thermal durability of Cu-CHA NH_3-SCR catalysts for diesel NO_x reduction, *Catal. Today*, 2012, **184**, 252–261.

6 S. Brandenberger, O. Kröcher, M. Casapu, A. Tissler and R. Althoff, Hydrothermal deactivation of Fe-ZSM-5 catalysts for the selective catalytic reduction of NO with NH_3, *Appl. Catal., B*, 2011, **101**, 649–659.

7 X. Shi, F. Liu, L. Xie, W. Shan and H. He, NH_3-SCR performance of fresh and hydrothermally aged Fe-ZSM-5 in standard and fast selective catalytic reduction reactions, *Environ. Sci. Technol.*, 2013, **47**, 3293–3298.

8 C. U. I. Odenbrand, $CaSO_4$ deactivated V_2O_5-WO_3/TiO_2 SCR catalyst for a diesel power plant. Characterization and simulation of the kinetics of the SCR reactions, *Appl. Catal., B*, 2018, **234**, 365–377.

9 H. Liu, C. You and H. Wang, Experimental and density functional theory studies on the zeolite-based Fe-Ni-W trimetallic catalyst for high-temperature NO_x selective catalytic reduction: Identification of active sites suppressing ammonia over-oxidation, *ACS Catal.*, 2021, **11**, 1189–1201.

10 L. Gang, B. Anderson, J. Van Grondelle and R. Van Santen, Low temperature selective oxidation of ammonia to nitrogen on silver-based catalysts, *Appl. Catal., B*, 2003, **40**, 101–110.

11 B. Bahrami, V. G. Komvokis, M. S. Ziebarth, O. S. Alexeev and M. D. Amiridis, NH_3 decomposition and oxidation over noble metal-based FCC CO combustion promoters, *Appl. Catal., B*, 2013, **130**, 25–35.

12 Y. Tian, Z. Han, Z. Zhou, H. Zhao, Q. Zeng, Y. Li and D. Ma, Synthesis of Cu/$CeTiO_x$ tandem catalyst with dual-function sites for selective catalytic oxidation of ammonia, *Chem. Eng. J.*, 2025, **503**, 158212.

13 X. Yang, B. Zhao, Y. Zhuo, Y. Gao, C. Chen and X. Xu, DRIFTS study of ammonia activation over CaO and sulfated CaO for NO reduction by NH_3, *Environ. Sci. Technol.*, 2011, **45**, 1147–1151.

14 G. Novell-Leruth, J. M. Ricart and J. Pérez-Ramírez, Pt(100)-catalyzed ammonia oxidation studied by DFT: Mechanism and microkinetics, *J. Phys. Chem. C*, 2008, **112**, 13554–13562.

15 Y. Yang, J. Liu, F. Liu, Z. Wang, J. Ding and H. Huang, Reaction mechanism for NH_3-SCR of NO_x over $CuMn_2O_4$ catalyst, *Chem. Eng. J.*, 2019, **361**, 578–587.

16 X. Li, K. Li, Y. Peng, X. Li, Y. Zhang, D. Wang, J. Chen and J. Li, Interaction of phosphorus with a $FeTiO_x$ catalyst for selective catalytic reduction of NO_x with NH_3: Influence on surface acidity and SCR mechanism, *Chem. Eng. J.*, 2018, **347**, 173–183.

17 Y. J. Kim, H. J. Kwon, I. Heo, I.-S. Nam, B. K. Cho, J. W. Choung, M.-S. Cha and G. K. Yeo, Mn-Fe/ZSM5 as a low-temperature SCR catalyst to remove NO_x from diesel engine exhaust, *Appl. Catal., B*, 2012, **126**, 9–21.

18 M. Zhu, J.-K. Lai, U. Tumuluri, Z. Wu and I. E. Wachs, Nature of active sites and surface intermediates during SCR of NO with NH_3 by supported V_2O_5-WO_3/TiO_2 catalysts, *J. Am. Chem. Soc.*, 2017, **139**, 15624–15627.

19 P. Gong, J. Xie, D. Fang, D. Han, F. He, F. Li and K. Qi, Effects of surface physicochemical properties on NH_3-SCR activity of MnO_2 catalysts with different crystal structures, *Chin. J. Catal.*, 2017, **38**, 1925–1934.

20 P. S. Hammershøi, P. N. R. Vennestrøm, H. Falsig, A. D. Jensen and T. V. W. Janssens, Importance of the Cu oxidation state for the SO_2-poisoning of a Cu-SAPO-34 catalyst in the NH_3-SCR reaction, *Appl. Catal., B*, 2018, **236**, 377–383.

21 Q. Zhang, T. Zhang, F. Xia, Y. Zhang, H. Wang and P. Ning, Promoting effects of acid enhancing on N_2 selectivity for selectivity catalytic oxidation of NH_3 over RuO_x/TiO_2: The mechanism study, *Appl. Surf. Sci.*, 2020, **500**, 144044.

22 Q. Zhao, B. Chen, J. Li, X. Wang, M. Crocker and C. Shi, Insights into the structure-activity relationships of highly efficient CoMn oxides for the low temperature NH_3-SCR of NO_x, *Appl. Catal., B*, 2020, **277**, 119215.

23 B. E. R. Snyder, M. L. Bols, H. M. Rhoda, D. Plessers, R. A. Schoonheydt, B. F. Sels and E. I. Solomon, Cage effects

© 2025 The Author(s). Co-published by the Institute of Process Engineering, Chinese Academy of Sciences and the Royal Society of Chemistry

Open Access Article. Published on 15 December 2025. Downloaded on 2/5/2026 10:57:16 PM. This article is licensed under a Creative Commons Attribution-NonCommercial 3.0 Unported Licence.

control the mechanism of methane hydroxylation in zeolites, *Science*, 2021, **373**, 327–331.

24 L.-C. Wang, Y. Zhang, J. Xu, W. Diao, S. Karakalos, B. Liu, X. Song, W. Wu, T. He and D. Ding, Non-oxidative dehydrogenation of ethane to ethylene over ZSM-5 zeolite supported iron catalysts, *Appl. Catal., B*, 2019, **256**, 117816.

25 S. Takenaka, Formation of filamentous carbons over supported Fe catalysts through methane decomposition, *J. Catal.*, 2004, **222**, 520–531.

26 T. P. Almeida, T. Kasama, A. R. Muxworthy, W. Williams, L. Nagy, T. W. Hansen, P. D. Brown and R. E. Dunin-Borkowski, Visualized effect of oxidation on magnetic recording fidelity in pseudo-single-domain magnetite particles, *Nat. Commun.*, 2014, **5**, 5154.

27 F. Jin, B. Wang, Y. Ning, Z. Zhang, J. Yang, H. Zhang, D. Wang and Y. Zhou, Graphene-modified mesoporous iron phosphate as superior binary sulfur host for lithium-sulfur batteries, *Energy Technol.*, 2020, **8**, 1901462.

28 Z. Xu, L. Zhang, M. Pan, Q. Jiang, Y. Huang, F. Wang and X. Liu, A bionanozyme with ultrahigh activity enables spatiotemporally controlled reactive oxygen species generation for cancer therapy, *Adv. Funct. Mater.*, 2021, **31**, 2104100.

29 F. O. Boakye, M. Fan, F. Zhang, H. Tang, R. Zhang and H. Zhang, Growth of branched heterostructure of nickel and iron phosphides on carbon cloth as electrode for hydrogen evolution reaction under wide pH ranges, *J. Solid State Electrochem.*, 2022, **26**, 875–885.

30 S. Bi, Z. Geng, Y. Wang, Z. Gao, L. Jin, M. Xue and C. Zhang, Multi-stage porous nickel-iron oxide electrode for high current alkaline water electrolysis, *Adv. Funct. Mater.*, 2023, **33**, 2214792.

31 R. Kumar, M. Mooste, Z. Ahmed, S. Akula, I. Zekker, M. Marandi, M. Käärik, J. Leis, A. Kikas, A. Treshchalov, M. Otsus, J. Aruväli, V. Kisand, A. Tamm and K. Tammeveski, Highly active ZIF-8@CNT composite catalysts as cathode materials for anion exchange membrane fuel cells, *Ind. Chem. Mater.*, 2023, **1**, 526–541.

32 Y. Shaharyar, J. Y. Cheng, E. Han, A. Maron, J. Weaver, J. Marcial, J. S. McCloy, A. Goel and L. Pinckney, Elucidating the effect of iron speciation (Fe^{2+}/Fe^{3+}) on crystallization kinetics of sodium aluminosilicate glasses, *J. Am. Ceram. Soc.*, 2016, **99**, 2306–2315.

33 X. Zuo, X. Wang, G. Si, D. Zhang, X. Yu, Z. Guo and N. Gu, Size-dependent oxygen vacancy of iron oxide nanoparticles, *Small Methods*, 2025, **9**, e2400685.

34 Y. Zhou, D. Wang, Y. Li, L. Jing, S. Li, X. Chen, B. Zhang, W. Shuai, R. Tao, X. Lu and J. Liu, Critical effect of oxygen pressure in pulsed laser deposition for room temperature and high performance amorphous In-Ga-Zn-O thin film transistors, *Nanomaterials*, 2022, **12**, 4358.

35 Y. Wu, X. Wu, J. Fan, H. Wang and Z. Wu, Insights into the roles of different iron species on zeolites for N_2O selective catalytic reduction by CO, *Environ. Sci. Technol.*, 2024, **58**, 22583–22593.

36 Q. Deng, R. Zhou, Y. C. Zhang, X. Li, J. Li, S. Tu, G. Sheng, J. Wang, Z. Zeng and T. Yoskamtorn, H^+-H^- pairs in partially oxidized MAX phases for bifunctional catalytic conversion of furfurals into linear ketones, *Angew. Chem.*, 2023, **135**, e202211461.

37 F. Qin, X. Fan and W. Ma, Selective oxidation of triethylamine catalyzed by Mn-Ce/ZSM-5, *Langmuir*, 2023, **39**, 7820–7830.

38 X.-Y. Peng, L.-J. Liu, B.-X. Shen, Y. Bian and L.-C. Su, Insight into the catalytic oxidation of toluene over M/ZSM-5 (M = Cu, Mn, Fe, Ce, Ti) catalysts, *J. Fuel Chem. Technol.*, 2023, **51**, 841–851.

39 J. Luo, K. Kamasamudram, N. Currier and A. Yezerets, NH_3-TPD methodology for quantifying hydrothermal aging of Cu/SSZ-13 SCR catalysts, *Chem. Eng. Sci.*, 2018, **190**, 60–67.

40 Y. Yu, X. Yi, J. Zhang, Z. Tong, C. Chen, M. Ma, C. He, J. Wang, J. Chen and B. Chen, Application of $ReOx/TiO_2$ catalysts with excellent SO_2 tolerance for the selective catalytic reduction of NO_x by NH_3, *Catal. Sci. Technol.*, 2021, **11**, 5125–5134.

41 X. Zhong, J. Liu, L. Gao, J. Chen, X. Wang, Y. Zhang, Y. A. Wu, M. Shakeri, X. Zhang and B. Zhang, Constructing the Al deficiency in Si-O(H)-Al units based on Pt/ZSM-5 for enhanced hydrocracking of polyethylene into high-quality liquid fuel, *Nano Res.*, 2024, **17**, 10088–10098.

42 K. Krishna, G. Seijger, C. Van Den Bleek, M. Makkee, G. Mul and H. Calis, Selective catalytic reduction of NO with NH_3 over Fe-ZSM-5 catalysts prepared by sublimation of $FeCl_3$ at different temperatures, *Catal. Lett.*, 2003, **86**, 121–132.

43 J. Zeng, S. Chen, Z. Fan, C. Wang, H. Chang and J. Li, Simultaneous selective catalytic reduction of NO and N_2O by NH_3 over Fe-Zeolite catalysts, *Ind. Eng. Chem. Res.*, 2020, **59**, 19500–19509.

44 H. Chang, T. Zhang, H. Dang, X. Chen, Y. You, J. W. Schwank and J. Li, Fe_2O_3@SiTi core-shell catalyst for the selective catalytic reduction of NO_x with NH_3: Activity improvement and HCl tolerance, *Catal. Sci. Technol.*, 2018, **8**, 3313–3320.

45 W. Kwiatek, A. Hanson, C. Paluszkiewicz, M. Gałka, M. Gajda and T. Cichocki, Application of SRIXE and XANES to the determination of the oxidation state of iron in prostate tissue sections, *J. Alloys Compd.*, 2004, **362**, 83–87.

46 S. Pongha, B. Seekoaon, W. Limphirat, P. Kidkhunthod, S. Srilomsak, Y.-M. Chiang and N. Meethong, XANES investigation of dynamic phase transition in olivine cathode for Li-ion batteries, *Adv. Energy Mater.*, 2015, **5**, 1500663.

47 J. Zhu, C. Jin, Y. Duan, L. Zhu, J. Liu, K. Cheng, H. Cheng, F. Liu, H. Li and J. Liu, Fe-triggered Mn-mullite oxides for efficient low-temperature reduction of nitrogen oxides: Insights into the structure-activity relationship, *Appl. Catal., B*, 2025, **366**, 125028.

48 Y. Wang, J. Han, M. Chen, W. Lv, P. Meng, W. Gao, X. Meng, W. Fan, J. Xu, W. Yan and J. Yu, Low-silica Cu-CHA zeolite enriched with Al pairs transcribed from silicoaluminophosphate seed: Synthesis and Ammonia performance, *Angew. Chem., Int. Ed.*, 2023, **62**, e202306174.

© 2025 The Author(s). Co-published by the Institute of Process Engineering, Chinese Academy of Sciences and the Royal Society of Chemistry

Open Access Article. Published on 15 December 2025. Downloaded on 2/5/2026 10:57:16 PM.
This article is licensed under a Creative Commons Attribution-NonCommercial 3.0 Unported Licence.

49 Q. Liang, X. Wu, D. Weng and H. Xu, Oxygen activation on Cu/Mn-Ce mixed oxides and the role in diesel soot oxidation, *Catal. Today*, 2008, **139**, 113–118.
50 X. Ding, J. Qiu, Y. Liang, M. Zhao, J. Wang and Y. Chen, New insights into excellent catalytic performance of the Ce-modified catalyst for NO oxidation, *Ind. Eng. Chem. Res.*, 2019, **58**, 7876–7885.
51 H. Kubota, C. Liu, T. Toyao, Z. Maeno, M. Ogura, N. Nakazawa, S. Inagaki, Y. Kubota and K.-I. Shimizu, Formation and reactions of NH_4NO_3 during transient and steady-state NH_3-SCR of NO_x over H-AFX zeolites: Spectroscopic and theoretical studies, *ACS Catal.*, 2020, **10**, 2334–2344.
52 P. E. Fanning and M. A. Vannice, A DRIFTS study of Cu-ZSM-5 prior to and during its use for N_2O decomposition, *J. Catal.*, 2002, **207**, 166–182.
53 L. Jia, L. Zhang, B. Liu, H. Cheng, H. Li, Z. Zhao, W. Zhu, W. Song, J. Liu and J. Liu, Interface induced by hydrothermal aging boosts the low-temperature activity of Cu-SSZ-13 for selective catalytic reduction of NO_x, *Environ. Sci. Technol.*, 2024, **58**, 15038–15051.
54 J. Liu, Y. Pan, Y. Duan, S. Liang, H. Cheng, M. Hua, X. Dai, F. Liu, H. Li and J. Liu, $Fe_{1-y}MnyZr_4O_x$ solid solution for efficient low-temperature selective catalytic reduction of NO_x, *Chem. Eng. Sci.*, 2025, **313**, 121750.
55 J. Cheng, D. Zheng, G. Yu, R. Xu, C. Dai, N. Liu, N. Wang and B. Chen, N_2O catalytic decomposition and NH_3-SCR coupling reactions over Fe-SSZ-13 catalyst: Mechanisms and interactions unraveling via experiments and DFT calculations, *ACS Catal.*, 2023, **13**, 934–947.
56 B. Ravel and M. Newville, ATHENA, ARTEMIS, HEPHAESTUS: Data analysis for X-ray absorption spectroscopy using IFEFFIT, *J. Synchrotron Radiat.*, 2005, **12**, 537–541.
57 H. Funke, A. Scheinost and M. Chukalina, Wavelet analysis of extended X-ray absorption fine structure data, *Phys. Rev. B: Condens. Matter Mater. Phys.*, 2005, **71**, 232–234.
58 W. Eijima, G. Shibata, N. Shibayama, Y. Kobashi, H. Ogawa and K.-I. Shimizu, Kinetic modeling of steady-state NH_3-SCR over a monolithic Cu-CHA catalyst, *Catal. Today*, 2020, **352**, 237–242.
59 P. S. Metkar, M. P. Harold and V. Balakotaiah, Experimental and kinetic modeling study of NH_3-SCR of NO_x on Fe-ZSM-5, Cu-chabazite and combined Fe- and Cu-zeolite monolithic catalysts, *Chem. Eng. Sci.*, 2013, **87**, 51–66.
60 S. Kiil, S. K. Bhatia and K. Dam-Johansen, Modelling of catalytic oxidation of NH_3 and reduction of NO on limestone during sulphur capture, *Chem. Eng. Sci.*, 1996, **51**, 587–601.

© 2025 The Author(s). Co-published by the Institute of Process Engineering, Chinese Academy of Sciences and the Royal Society of Chemistry